Solid State Ionics 411 (2024) 116569

Contents lists available at ScienceDirect

Solid State Ionics

journal homepage: www.elsevier.com/locate/ssi

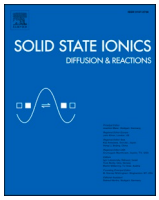

Enhancing LSCF-based air electrode durability: Insights into sulfur poisoning and air purification

Yousef Alizad Farzin [a,*], Michael Harenbrock [b], David Nardini [c], André Weber [a]

[a] Institute for Applied Materials - Electrochemical Technologies (IAM-ET), Karlsruhe Institute of Technology (KIT), Adenauerring 20b, 76131 Karlsruhe, Germany
[b] MANN+HUMMEL GmbH, Schwieberdinger Str. 126, 71636 Ludwigsburg, Germany
[c] MANN+HUMMEL Innenraumfilter GmbH & Co. KG, Kulmbacher Straße 12, 95502 Himmelkron, Germany

ARTICLE INFO

Keywords:
LSCF-GDC air electrode
Sulfur poisoning
Air purification
Degradation mechanisms
Electrochemical performance

ABSTRACT

The electrochemical performance of perovskite-type air electrodes in solid oxide cells is strongly affected by a trace amount of SO_2 as the air impurity. The present work aims to study air purification efficiency in suppressing the degradation rate for the LSCF-GDC air electrode while operating under different SO_2 concentrations. For this purpose, the electrochemical performance of symmetrical cells was evaluated using impedance spectra measured over 320 h and compared with intrinsic electrode degradation in synthetic air. Accordingly, the intrinsic degradation rate was measured at 0.05 mΩ cm^2 h^{-1} while exposing the cell to synthetic air containing 10 and 100 ppb SO_2, causing a severe increase to 0.17 and 0.30 mΩ cm^2 h^{-1}, respectively. Nevertheless, the calculated degradation rate under purified air containing 100 ppb SO_2 was similar to the LSCF-GDC intrinsic degradation rate, representing the high practicality of filter material to adsorb SO_2 species. Interpreting the impedance spectra using a distribution of relaxation times (DRT) and a complex nonlinear least squares fit (CNLS) revealed that the intrinsic degradation mechanisms were the limitation of dissociative surface adsorption of oxygen and charge transfer to the adsorbed oxygen. At the same time, inhibition of the O_2 adsorption caused by the deposition of SrO, SO_3^{2-}, and $SrSO_4$ phases and increasing surface diffusion resistance for the adsorbed oxygen atoms were the rate-determining steps in SO_2-containing synthetic air. Lastly, the effective suppression of degradation rate by gas purification indicates an extensive use of filter material to extend the lifespan of SOCs.

1. Introduction

In recent decades, global energy consumption has significantly increased greenhouse gas emissions. A significant amount of attention has been paid to the development and utilization of renewable energy sources in order to address this issue. Power-to-X technology has emerged as a promising solution, enabling renewable power conversion into storable and transportable fuels and chemicals. These include hydrogen, methane, ammonia, and dimethyl ether [1].

Solid oxide cells (SOCs) are electrochemical devices crucial in energy conversion. They can convert chemical energy into electricity (known as solid oxide fuel cells, SOFCs) or electricity into different fuels (known as solid oxide electrolysis cells, SOECs) with remarkable efficiency [2–4]. Typical materials for SOCs are zirconia doped with yttria (YSZ) for the dense electrolyte, a porous cermet of nickel and YSZ (Ni-YSZ cermet) for the fuel electrode, and mixed ionic and electronic conductors (MIECs) for the air electrode. The use of MIECs allows for extending the electrochemically active region to the whole electrode surface instead of being limited to three-phase boundaries (TPBs), which can promote electrode performance for oxygen reduction reaction (ORR).

Among the different compounds for the air electrode, lanthanum strontium cobalt ferrite (La, Sr)(Co, Fe)$O_{3-\delta}$ (LSCF) is known as the state-of-the-art air electrode for SOCs application [5]. It exhibits excellent chemical stability, high ionic and electronic conductivity, high catalytic activity toward the oxygen reduction reaction, and an acceptable thermal expansion coefficient [6]. The LSCF electrode, with its perovskite structure and high ambipolar conductivity, provides active reaction sites beyond the traditional TPB. A general drawback of most Sr-containing perovskites, such as LSC and LSCF, is the chemical incompatibility with the state-of-the-art YSZ electrolyte. The direct contact during sintering or cell operation leads to an insulating strontium zirconate layer, which is commonly suppressed by an interlayer of doped ceria [7,8].

A high oxygen surface exchange and oxygen diffusion coefficient are two crucial characteristics of air electrode materials for achieving a

* Corresponding author.
E-mail address: yousef.farzin@kit.edu (Y. Alizad Farzin).

https://doi.org/10.1016/j.ssi.2024.116569
Received 11 March 2024; Received in revised form 11 April 2024; Accepted 22 April 2024
Available online 26 April 2024

desirable performance [9]. The significant advantages of LSCF perovskite over other perovskite electrodes are its significantly higher oxygen diffusion and surface exchange properties [5]. However, its electrochemical performance is inhibited primarily by deactivating the electrode surface during long-term operation. The degradation of surface kinetics is caused by various ageing phenomena activated by material instabilities, especially at surfaces and trace amounts of impurities in the air [10]. One notable degradation mechanism involves the segregation of strontium (Sr) cations to the electrode surface, leading to the formation of non-electrocatalytically active SrO phases. The concentration of SrO increases with elevated operating temperatures and decreased oxygen partial pressure [11,12].

On the other hand, the kinetic of SrO formation and its influence on electrochemical performance degradation highly depends on the LSCF chemical composition and operation condition [13,14]. Unfortunately, finding a practical solution to mitigate Sr segregation remains challenging due to energy minimization and charge interactions resulting from the lattice mismatch between the host La^{3+} cations and the dopant Sr^{2+} cations [5].

The segregated SrO phase can react with air contaminants such as sulfur dioxide (SO_2) and carbon dioxide (CO_2) to form the $SrSO_4$ and $SrCO_3$ phases, respectively. The reactions' kinetic for the deposition of sulfur and formation of $SrSO_4$ get accelerated by operating the cell above 700 °C [15]. The formation of $SrSO_4$, called sulfur poisoning, was recognized in the air electrode operated at the ppm level of SO_2 by the AIST group via secondary ion mass spectrometry (SIMS) [16,17]. Although SO_2 concentrations in ambient air are as low as just a few parts per billion (ppb), such SO_2 can still be capable of degrading cell/stack performance and shortening their lifetime during long-term operation [11,18].

It is suspected that the formation of $SrSO_4$ and the rate of cell performance degradation are closely related to the concentration of SO_2, suggesting that increasing the SO_2 concentration could accelerate degradation. Budiman et al. [19] have investigated the surface chemistry of the LSCF air electrode under 10 ppb sulfur-containing air. It was found that the reaction of LSCF with SO_2 leads to the formation of $SrSO_4$ and $CoFe_2O_4$, resulting in changes in surface composition followed by increasing polarization resistance. The variation in surface chemical composition affects the corresponding electrochemical reactions by reducing the surface exchange coefficient. As an example, after exposing the LSCF electrode to 20 ppm SO_2 for 48 h, the electrical conductivity relaxation experiments indicated that the surface exchange coefficient decreased from 2.8×10^{-4} to 9×10^{-5} cm s^{-1} at 700 °C and from 5×10^{-4} to 8×10^{-6} cm s^{-1} at 800 °C [15].

As the surface chemical composition evolves, it can also impact the ionic conductivity of the LSCF electrode. Wang et al. [20] demonstrated that increasing the SO_2 concentration above 10 ppm caused approaching the $La_{0.6}Sr_{0.4}Co_{0.2}Fe_{0.8}O_3$ chemical composition to $LaFeO_3$ after forming $SrSO_4$ and $CoFe_2O_4$ phases and the number of oxide ion vacancies decreased consequently. The reduced availability of oxygen vacancies hinders the mobility of oxygen ions, impeding their transport through the electrode. Therefore, this limits the overall efficiency and performance of the cell.

Nevertheless, the main factor responsible for the degradation of the electrochemical performance of LSCF in an SO_2-containing air atmosphere has been identified as the reaction of SO_2 with SrO to form $SrSO_4$ [19]. It means that the poisoning of the air electrode caused by sulfur in the supplied air cannot be negated during the long-term operation of SOFCs. Different solutions have been proposed in the literature against sulfur poisoning of air electrodes. By modifying electrode material and creating a sulfur trapping area, a protective layer can be designed along the air channel to ensure the trapping part of capturing SO_2 is achieved by the chemical reaction of air electrode materials. The (La, Sr)$CoO_{3-\delta}$ (LSC) is the most typical solution because its reactivity is the most significant. Adding additive components to air electrode material is another approach that can be used to improve sulfur tolerance. It involves the application of a Mg/Fe layer to capture sulfur species and impregnate BaO and $BaCeO_3$ to improve sulfur tolerance [21–23]. By forming $BaSO_4$ instead of $SrSO_4$, excess Sr and Co deficiency is prevented within LSCF perovskite.

Developing a Sr-free material as an alternative air electrode may exhibit high sulfur tolerance. The sulfur poisoning behaviour of calcium-doped $Pr_{0.8}Ca_{0.2}FeO_{3-\delta}$ and $La_{0.8}Ca_{0.2}FeO_{3-\delta}$ are the two most common candidates studied for this purpose, even though the stabilization of calcium perovskite is less than that of the strontium-doped perovskite [24,25]. However, the results showed no drastic changes in their reactivity with sulfur by forming $CaSO_4/Pr_2(SO_4)_3$ instead of $SrSO_4/La_2O_2SO_4$.

As a practical solution to purify the inlet air, filters and more advanced air purification systems are commonly employed in fuel cell systems to prevent poisoning and subsequent degradation of fuel cell stacks [26]. Similarly, this study evaluates the applicability of such filters to the LSCF-GDC composite air electrode in an electrolyte-supported cell (ESC). The filter used in this study consists of specially modified activated carbons designed to remove SO_2 and other air impurities. As a first step, the intrinsic degradation rate of the LSCF-GDC electrode was investigated under synthetic air. Subsequently, similar tests were conducted using synthetic air containing different SO_2 concentrations to study the degradation mechanism induced by ambient air impurities and compare it to those obtained for purified SO_2-containing air. The primary objective of this work is to evaluate the effectiveness of the filter material in suppressing the degradation rate of the LSCF-GDC air electrode after identifying rate-determining steps in the oxygen reduction reaction.

2. Experimental

Symmetrical cells based on a 3YSZ electrolyte containing a GDC barrier layer and LSCF-GDC air electrode were subjected to study the degradation mechanisms and rate under different SO_2 concentrations. The symmetrical LSCF-GDC cells with an active electrode surface area of 1 cm^2 and electrolyte size of 2.5 cm^2 were provided by Sunfire GmbH, Dresden 01237, Germany.

The symmetrical cells were investigated by impedance spectroscopy, and all spectra were measured under OCV conditions in a test bench as described in [27]. In order to determine the rate-determining reaction in the electrochemical performance of the LSCF-GDC electrode, impedance spectra have been recorded at the temperature range of 660–750 °C under the mixture of O_2 and N_2 in different volume ratios. The synthetic air was prepared by mixing 21 vol% oxygen (99.95% O_2; the main impurities were H_2O and Ar) and 79 vol% nitrogen (99.999% N_2) provided by the Air Liquide company. After investigating electrode performance at different temperatures, the testing temperature was kept at 750 °C for 360 h to study the intrinsic degradation mechanisms under synthetic air. During this period, the impedance of the electrode was measured every two hours.

The degradation phenomena resulting from air impurities were then investigated using synthetic air containing 10 and 100 ppb SO_2 under similar testing conditions. Furthermore, an additional filter layer was applied between the mass flow controller and the cell housing to assess its effectiveness in adsorbing sulfur from subjected gases. The developed filter (MANN+HUMMEL Innenraumfilter GmbH & Co. KG, 95502 Himmelkron, Germany) with modified activated carbons is designed to remove air impurities at ambient temperature and pressure. The active area of the filter was 0.95 cm^2, corresponding to an air velocity of 0.088 m s^{-1} at an airflow rate of 500 sccm (standard cubic centimeters per minute).

The microstructure of the subjected electrode was examined with a scanning electron microscope (Zeiss SEM 1540 XB). The postmortem analysis was conducted using a focused ion beam (FIB/SEM) equipped with Everhart-Thornley and in-lens detectors (1.3 and 4 kV acceleration voltage) to identify sulfur species in the electrode structure after 320 h of

operation. The impedance spectra were recorded using a Zahner Zennium Pro frequency response analyzer, in which the frequency range was 10 mHz to 500 kHz with a voltage amplitude of 12 mV. As the measurements were conducted on symmetrical cells, the measured area-specific polarization resistance (ASR) value obtained was divided by two.

The impedance spectra were analyzed using the distribution of relaxation times (DRT) [28] to identify the processes in the LSCF-GDC electrode, which was then combined with a complex nonlinear least squares (CNLS) fit to interpret the impedance data.

3. Results and discussion

3.1. Microstructure investigation

Fig. 1 shows the SEM images of the LSCF-GDC composite air electrode in an electrolyte-supported cell configuration. The investigated cell consists of a 3YSZ electrolyte with a thickness of 80 μm, which provides a mechanically robust cell. Moreover, an intermediate barrier layer of GDC is applied to the 3YSZ electrolyte with a thickness of approximately 5 μm. As the GDC barrier layer is chemically compatible with the electrolyte and electrode material, it prevents the formation of the insulating $SrZrO_3$ phase. In addition, GDC in the active LSCF electrode layer can improve the charge transfer reaction by extending the LSCF/GDC interface and accelerating the oxygen ion diffusion through the electrode bulk. The outer layer is constructed with a combination of composite LSCF-GDC and LSCF layers, which can optimize the electrode performance by providing high mechanical stability, oxide ion conductivity, and active surface sites. In the final layer, a layer of (La, Sr)(Mn, Co)O_3 is used as a contact layer to improve the current collection to the external circuit, which is made of gold mesh and wires.

It is apparent from the SEM image (Fig. 1) that there is a homogeneous distribution of open porosity throughout the entire electrode structure. The average pore size and porosity of the investigated LSCF-GDC electrode are estimated to be 500 nm and 38%, respectively. Combining open pores and sufficient porosity in the electrode microstructure can provide an adequate diffusion path for molecular oxygen, decrease gas diffusion resistance, and improve electrochemical performance [4].

Fig. 2 shows a FIB/SEM image together with EDS mapping analysis, including sulfur and primary cations of the LSCF-GDC composite air electrode following 320 h of operation in air containing 100 ppb SO_2. In the EDS image corresponding to the sulfur, it is evident that there is a high concentration of sulfur species at the (α) region, which is located close to the LSCF/(La, Sr)(Mn, Co)O_3 interface. Additionally, this region contains highly segregated Sr cations from the LSCF perovskite. Consequently, the electrode/gas interface was covered with SrO and $SrSO_4$ when the cell was operated at 750 °C for 320 h, a well-known degradation mechanism for Sr-containing perovskites.

The EDS images of the other cations for the LSCF electrode show a uniform distribution in the beneath layers, representing the chemical stability of perovskite bulk at 750 °C for the air side of the SOCs. Meanwhile, the concentration of sulfur species decreases toward the interface of the electrolyte/GDC barrier layer. The occupation of SO_2 in the oxide ion vacancies and subsequent formation of SO_3^{2-} is an irreversible poisoning effect of SO_2 for the perovskites with Sr in the A sites [29]. The apparent low concentration of S in this region is most likely due to the degradation of the LSCF grain surface and the deposition of an ultra-thin S layer before the formation of $SrSO_4$. Nevertheless, a detailed surface chemistry analysis requires advanced characterization techniques such as secondary ion mass spectrometry (SIMS), which is not the subject of our study.

The top-view SEM/EDS mappings of the pristine LSCF-GDC electrode and postmortem electrode after operation for 320 h in SCA-100 at 750 °C are shown in Fig. 3. The corresponding image for the pristine electrode shows the (La, Sr)(Mn, Co)O_3 layer, as a contact layer, with a relatively large particle in the range of 1–6 μm. Due to its high electronic conductivity, this layer establishes a durable electrical contact between the subjected cell and the external circuit. It also provides a stable microstructure with large pores for gas diffusion due to the large particle size, which does not tend to agglomerate during operation. The microstructural stability of the contact layer can also enhance the physical bonding between the cell and the outer circuit over a long period of operation [30].

In order to investigate microstructural evolution after a short-term test in SO_2-containing air, a top-view SEM analysis has been done for the (La, Sr)(Mn, Co)O_3 (Fig. 3b) and LSCF (Fig. 3c) layers. The analysis of the (La, Sr)(Mn, Co)O_3 layer shows the formation of SrO and (Sr, S)O_x with different morphologies. It is evident that the formation of $SrSO_4$ mainly causes a crystal structure change on the LSCF surface, resulting in an orthorhombic crystal structure with the Pnma space group [31]. Meanwhile, the segregation of SrO from the perovskite structure most likely coincides with the expansion of the backbone into the electrode pores.

The top-view microscopy image of the outer LSCF layer is shown in Fig. 3c. It is necessary to highlight that the electrode/gas interface

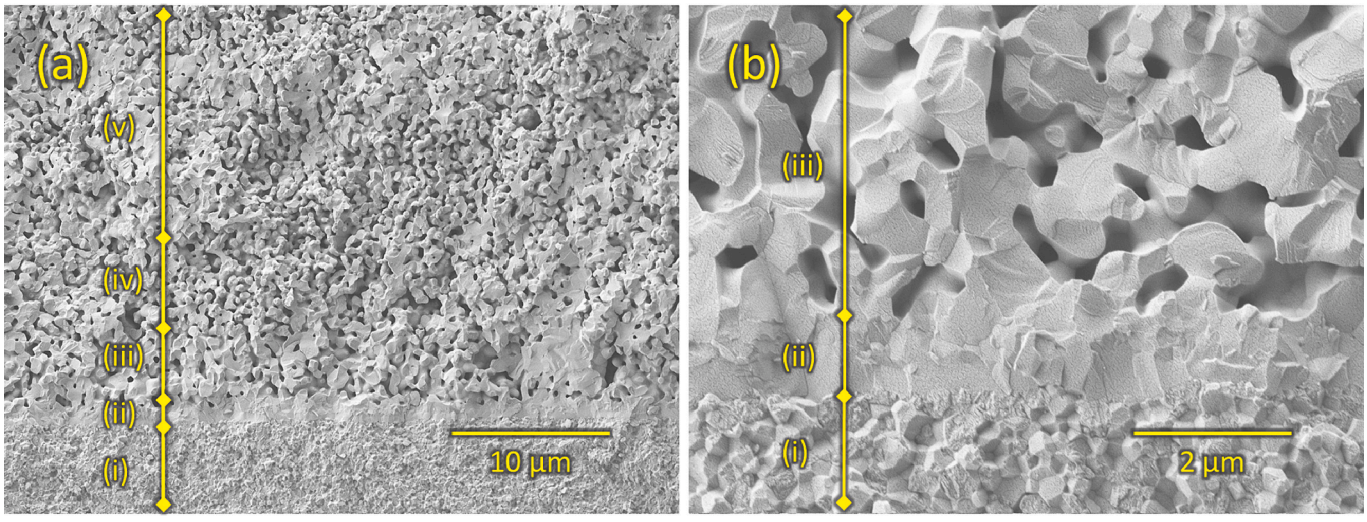

Fig. 1. Cross-section SEM images of the LSCF-GDC electrode in an electrolyte-supported cell (ESC) configuration at different magnifications (a and b). The images show (i) 3YSZ electrolyte, (ii) GDC dense barrier layer, (iii) GDC interdiffusion layer, (iv) LSCF-GDC composite layer, and (v) LSCF layer.

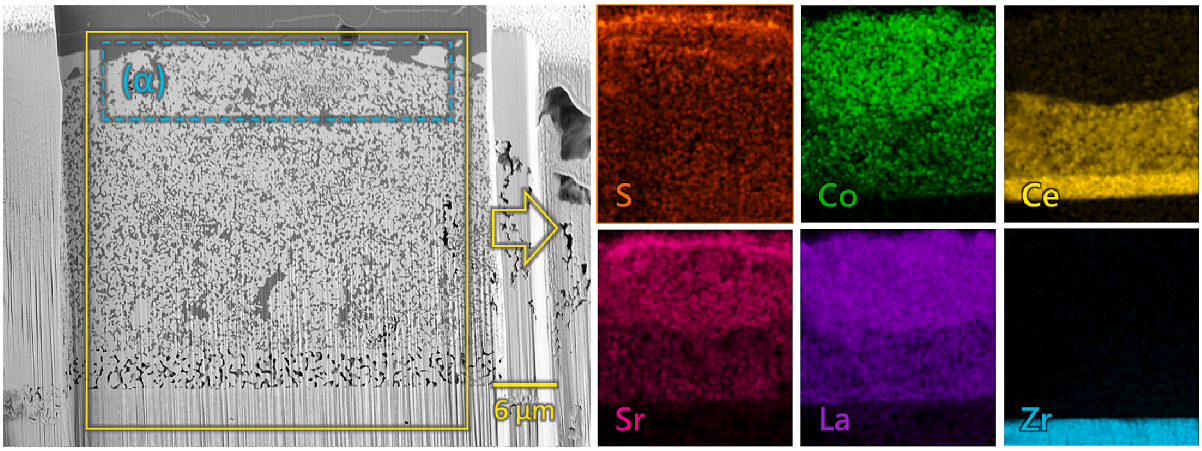

Fig. 2. Cross-section FIB/SEM image combined with elemental information from EDS mappings, including sulfur and primary cations of the LSCF-GDC electrode after operation for 320 h in 100 ppb sulfur-containing air (SCA-100) at 750 °C.

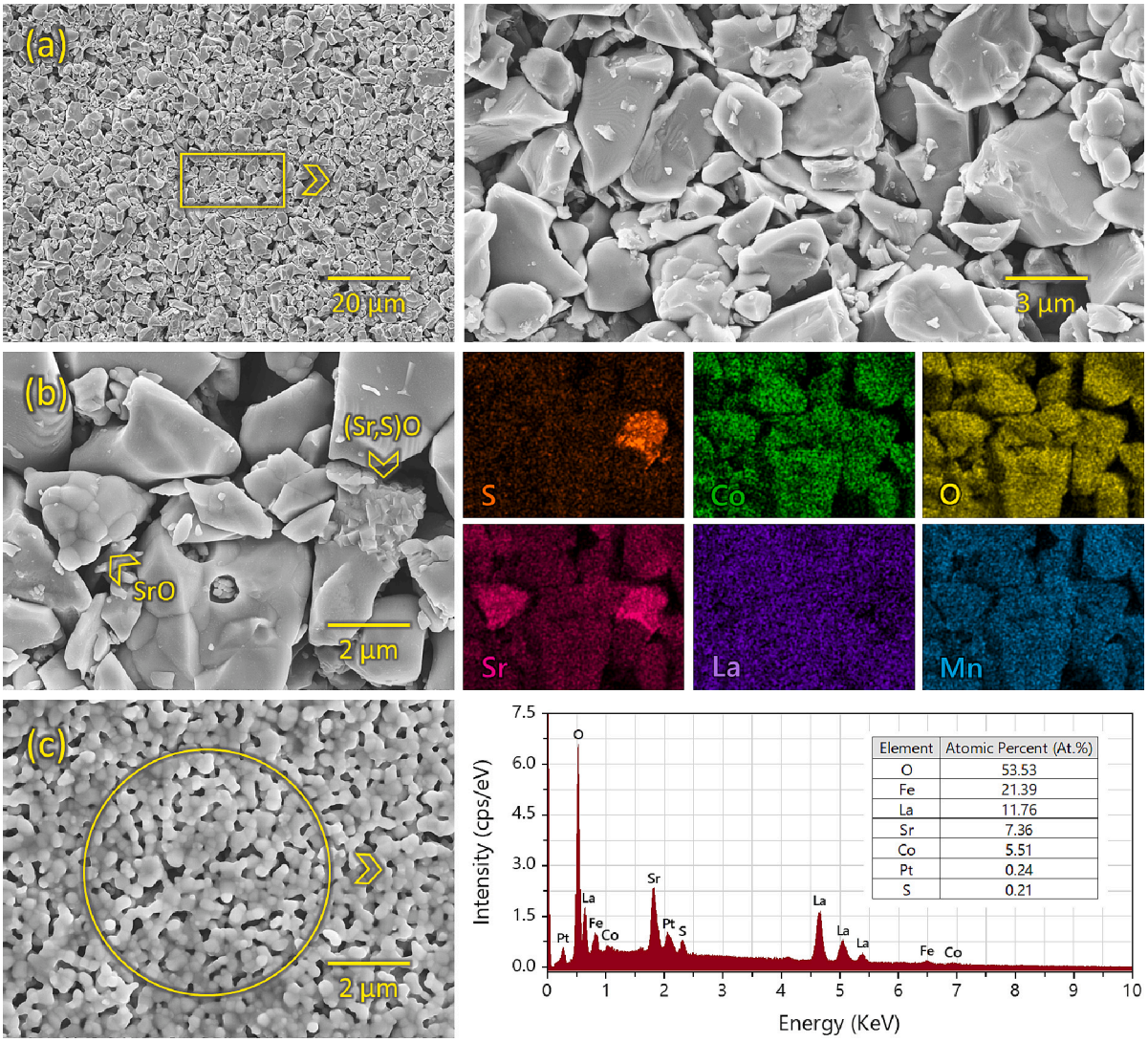

Fig. 3. Top-view SEM/EDS mappings of the LSCF-GDC electrode. (a) the (La, Sr)(Mn, Co)O_3 layer for pristine electrode and (b and c) postmortem image of the operated electrode for 320 h in 100 ppb sulfur-containing air (SCA-100) at 750 °C. Note: Figure (b) shows the top view image of the (La, Sr)(Mn, Co)O_3 layer, and (c) illustrates the beneath LSCF layer, which is under the (La, Sr)(Mn, Co)O_3 layer, after a short-term test with 100 ppb SO_2.

thermodynamically tends to form a denser layer compared with the beneath layers during cell processing. Accordingly, the mean pore size and porosity are estimated at 300 nm and 21%, respectively, lower than the corresponding values obtained from the cross-section image. Point EDS spectra show chemical species on LSCF electrodes, which have been collected from a large area (Fig. 3c). The Pt signals are caused by a thin layer of Pt applied before the microscopy study to enhance the surface electronic conductivity of the samples for improved image quality. The corresponding peak for the S with a concentration of 0.21 at.% represents the poisoning of the LSCF electrode under operation in SCA-100. As a result of SrO and $SrSO_4$ formation, blocking of the initially open pores was reported for $La_{0.6}Sr_{0.4}CoO_{3-\delta}$ electrode during annealing with minute traces of SO_2 due to Sr segregation to the surface [32]. Considering the SEM results (Figs. 2 and 3), blocking of gas diffusion due to the closure of pores can be excluded for the samples investigated in this study.

3.2. Electrochemical performance

The overview of the polarization resistance (R_p) and ohmic resistance (R_s) for the tested LSCF-GDC electrode at 750 °C and in different gas conditions are shown in Fig. 4. The R_s for the tested cells are all within a narrow range of 0.925 to 0.939 Ω cm^2. As a result of the short length of the wire used in the test setup design, the inductance contribution to the measurement data should be minimal. Notably, the release of the cations from LSCF associated with the reactivity at the zirconia-based electrolyte interface to form $SrZrO_3$ can contribute significantly to the overall degradation of cell performance. The degradation of the ohmic resistance has also been reported before for the cell containing a porose GDC barrier layer during operation for an extended period [33]. While operating for this period, the segregated SrO could form volatile species and diffuse within the porosity of the barrier layer, forming $SrZrO_3$ on the YSZ electrolyte. However, the results obtained in the current study illustrate the high practicality of the applied GDC layers, including a dense GDC barrier layer and porose GDC interdiffusion layer, to suppress the formation of the resistive phases at the electrode/electrolyte interface. On the other hand, by applying the GDC barrier layer, an interdiffusion layer can be formed between the GDC and YSZ layers, which is reported to have a lower conductivity [34] but still a minor impact on the series resistance of the cell [35,36].

In contrast to the ohmic resistance, the polarization resistance of the tested cells increases depending on the applied gases over the testing period. The exposure of the LSCF-GDC air electrode to sulfur-containing air (10 and 100 ppb SO_2 in synthetic air) causes a drastic degradation rate. Nevertheless, the obtained results for the tested cells in synthetic air and purified 100 ppb SO_2-containing air show the same degradation rate with a similar initial polarization resistance of about 0.057 Ω cm^2.

In order to make calling easier, we intend to use the abbreviation 'SA' for synthetic air, 'AA' for ambient air, 'SCA' for SO_2-containing air, and 'PA' for purified SO_2-containing air. The SCA gas consists of synthetic air with 10 ppb SO_2 (SCA-10) and 100 ppb SO_2 (SCA-100). In addition, the maximum concentration of SO_2 in synthetic air (SCA-100) is utilized in the purification test (PA) to investigate the practicality of the developed filter in adsorbing SO_2 as the main critical impurity in ambient air. The overview of the testing condition and gas composition are summarized in Table 1.

Based on the degradation rate at 750 °C, the electrochemical performance of the studied cells can be divided into two regions in Fig. 4. The first region, highlighted in red, shows a sharp increase of R_p for the AA, SCA-10, and SCA-100 cells during ageing for 70 h. At the same time, this degradation rate is moderated for both the SA and PA cells. The previous study observed this time-dependent degradation behaviour for ageing tests at 750 °C [13]. The difference in variation of polarization resistance indicates a high impact of SO_2 species on the early degradation rate and overall electrochemical performance of the LSCF-GDC electrode. Likely, the segregation of SrO and contamination of the surface of the LSCF grains are the primary mechanisms responsible for the early degradation of electrode performance in SA and PA cells. At the same time, air impurities such as CO_2 and SO_2 can accelerate the Sr segregation with favourable thermodynamics. Quick surface segregation of SrO, $SrSO_4$, $SrCO_3$, or deposition of SO_3^{2-} were also reported before for the (La, Sr)(Co, Fe)$O_{3-\delta}$ electrode at a similar temperature range of 650–750 °C [10,37].

After operating for about 70 h, in the second region with a yellow colour, the degradation rate of polarization resistance across all testing conditions started to decrease. Accordingly, the estimated degradation rate, determined by the slope of the SA and PA curves, relays at about 0.01 ± 0.003 mΩ cm^2 h^{-1} in its minimum. This similar degradation rate underscores the remarkable effectiveness of filter material in adsorbing SO_2 species from 100 ppb SO_2 containing synthetic air (SCA-100). In contrast, the degradation rate for the SCA-10 and SCA-100 cells remains

Table 1
Overview of the testing conditions and gas compositions used to investigate SO_2 poisoning for the LSCF-GDC air electrode at 750 °C. Note: The concentration of SO_2 for the ambient air is derived from the Federal Environment Agency website for Karlsruhe, where the experiments were conducted.

Cell ID	Gas composition	SO_2 concentration (ppb)	Gas purification
SA	Synthetic air	0	No
AA	Ambient air	0.4–1.2	No
SCA-10	Synthetic air + SO_2	10	No
SCA-100	Synthetic air + SO_2	100	No
PA	Synthetic air + SO_2	100	Yes

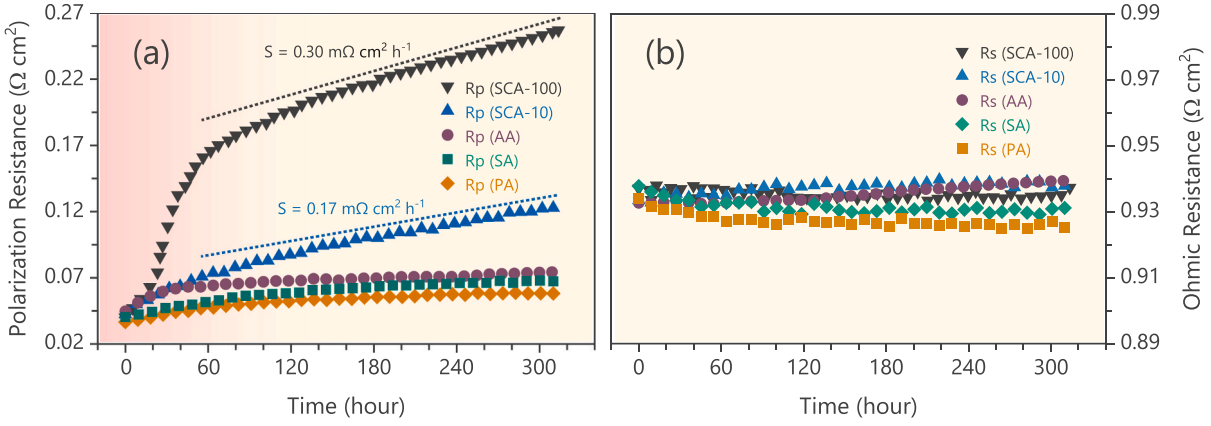

Fig. 4. The overview of (a) polarization resistance (R_p) and (b) ohmic resistance (R_s) for the tested LSCF-GDC composite air electrode at 750 °C in 100 ppb SO_2-containing air (SCA-100), 10 ppb SO_2-containing air (SCA-10), ambient air (AA), synthetic air (SA), and purified 100 ppb SO_2-containing air (PA).

relatively constant, with a high rate of increasing polarization resistance (to 0.17 mΩ cm^2 h^{-1} for SCA-10 and 0.30 mΩ cm^2 h^{-1} for SCA-100) during the investigation period, and only a slight initial decrease is observed for SCA-10.

Having examined the degradation rate for different gas compositions, we will interpret the impedance spectra and discuss the degradation mechanisms by fitting the Nyquist plots with an equivalent circuit model. Before interpreting the data, it is essential to note that different equivalent circuits have been proposed to model or fit Nyquist spectra for oxygen reduction reactions despite the LSCF perovskite being known as the state-of-the-art electrode for the air side of the solid oxide cells [38–40]. In those, the electrode microstructure, chemical compositions ($La_{1-x}Sr_xFe_{1-y}Co_yO_{3-\delta}$), and the layers forming the air side of the solid oxide cell have determining effects on the number of reactions and the polarization resistance [38,41].

A Gerischer-type impedance response was initially reported to describe the complex nature of mixed conducting porose SOC air electrodes [42]. As a diagnostic tool, it allows interpreting the impedance spectra for the air electrodes, such as $La_{0.6}Sr_{0.4}Co_{0.2}Fe_{0.8}O_{3-\delta}$ [38], $(La_{0.6}Sr_{0.4})_{0.99}CoO_{3-\delta}$ [43], and $La_{1-x}Sr_xCo_{1-y}Ni_yO_{3-\delta}$ [44]. The Gerischer element relies on the assumption of co-limited oxygen ion diffusion and surface reactions while associating an infinite diffusion length, which is fulfilled if the thickness of the electrode significantly exceeds the penetration depth [45]. Thus, its parameters obtainable from a CNLS-fit are directly related to oxygen surface exchange and oxygen ion diffusion coefficient through the bulk, which are the performance-relevant parameters of a mixed conducting air electrode. They can be quantified if the microstructural parameters of the electrode have been obtained from microstructure reconstructions [39].

Using the GDC with high ionic conductivity to make an LSCF-GDC composite air electrode in this work would contradict the criteria of using the Gerischer element to interpret the impedance spectra. A much more complex transmission line model (TLM) would be necessary to consider the coupling of surface reactions on LSCF surfaces and oxide ion diffusion through the LSCF and GDC particles, including LSCF/GDC interfaces in the composite electrode. The meaningful parameterization of a TLM requires a separate determination of parameters [46], which is challenging if O^{2-} transport occurs in two interpenetrating phases with different O^{2-} diffusion coefficients. For this reason, this work uses RQ elements rather than the Gerischer element to investigate the degradation mechanisms of the LSCF-GDC composite air electrode.

Fig. 5 illustrates the Nyquist plot and the distribution of relaxation times (DRT) in synthetic air (SA cell) at 750 °C. Note that the impedance spectra in the provided figures correspond to the polarization resistance of two LSCF-GDC electrodes in a symmetrical cell configuration and must be divided by two for one electrode. The impedance spectra were analyzed using in-house software to quantify the contributions of each reaction to the overall cell performance. The DRT method allows the deconvolution of electrochemical processes with relatively close time constants in porose electrodes, facilitating a better understanding of electrochemical reactions [47]. The DRT calculation incorporates many input values, including the frequency range of the DRT, the number of impedance values to be considered, the regularization parameter (λ), and the number of points per decade. These values are derived from a judgment of the residuals for the DRT calculation and user experience. However, the most important parameter of the DRT calculation is λ, which smoothes the profile and prevents artificial peaks. By choosing an optimal value for λ = 0.005 based on the impedance data quality, the number of individual processes with different relaxation frequencies has been identified and transferred to the Nyquist plot. It should be noted that the symmetrical cells exhibited ohmic resistances of about 0.93 Ω cm^2, whereas the initial polarization resistance of the LSCF-GDC electrode has been as low as 30 mΩ cm^2, a ratio impeding the data quality of the polarization resistance.

Based on the DRT plots, the overall impedance of the LSCF-GDC electrode contains five peaks that are attributed to five processes in series, including two high-frequency processes (HF, f > 10^4 Hz), two middle-frequency processes (MF, f = 100–30,000 Hz), and one low-frequency process (LF, f < 30 Hz). To quantify the individual processes, the following equivalent circuit model consisting of four RQ elements and a finite length Warburg element is fitted to the measured spectra.

$$R_0(R_1Q_1)(R_2Q_2)(R_3Q_3)(R_4Q_4)(FLW) \quad (1)$$

R_0 represents the ohmic resistance of two LSCF-GDC air electrodes in a symmetric configuration, 3YSZ electrolyte, and GDC barrier layers. Four R_nQ_n elements represent the processes related to the oxygen ion diffusion through the electrode bulk, oxygen dissociative surface adsorption, and interfacial and bulk transfer of charge. Besides, the unavoidable gas diffusion is represented by a Finite-Length-Warburg (FLW) element at low frequencies. The polarization resistance (R_p) is estimated by taking the sum of the R_nQ_n and FLW processes. More complex elements like transmission line modeling approaches were not applicable as the required microstructural parameters were unavailable for the investigated electrode.

The complexity of electrochemical reactions makes it challenging to correlate the individual peaks in the Nyquist plot to physicochemical processes. Despite this, the polarization resistance as a function of temperature and oxygen partial pressure is the most commonly used approach for determining the characteristic features of the limiting processes and attributing them to physicochemical phenomena such as charge transfer processes, solid-state diffusion, gas diffusion, and surface reactions [9,40].

Fig. 6 illustrates the dependency of impedance spectra, DRTs, and fitting results on the temperature. The real part of the spectra has been shifted by setting Re(Z(500 kHz)) = 0 to enable the comparison of polarization resistance for the obtained results. The DRT plots (Fig. 6b) and calculated activation energies (Fig. 6c) represent thermally-activated processes at high- and middle-frequency regions, while the low-frequency reaction (R_5) is a non-thermally activated process with similar polarization resistance of 0.011 ± 0.005 Ω cm^2 in the investigated temperature range (660–750 °C).

Fig. 7 shows the dependency of impedance spectra, DRTs, and fitting results on the oxygen concentration and obtained reaction orders (n_i) for the fit results. The pO_2 in a mixture of O_2 and N_2 gases varies from 0.002 to 0.5 atm. The fit for R_1Q_1 and R_2Q_2 at high frequencies indicates rather

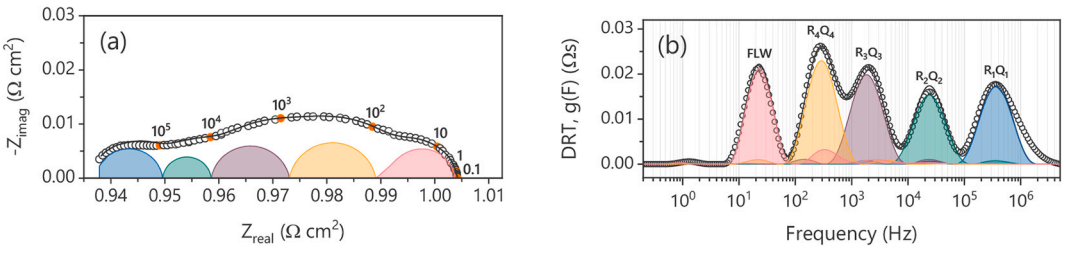

Fig. 5. The (a) Nyquist spectra and (b) distribution of relaxation times (DRT) of the LSCF-GDC air electrode at 750 °C in synthetic air (SA). Note: the polarization resistance is measured for two LSCF-GDC electrodes in a symmetrical cell configuration.

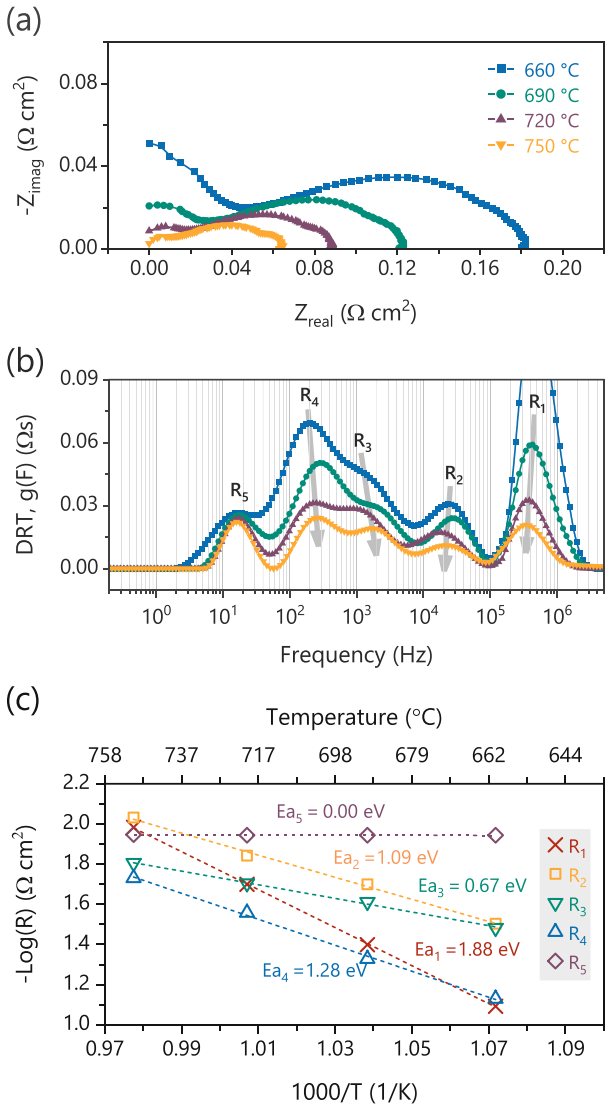

Fig. 6. Temperature dependency of (a) the impedance spectra, (b) corresponding DRTs, and (c) Arrhenius plots of fitted polarization processes of the LSCF-GDC composite air electrode. Note: the polarization resistance is measured for two electrodes in a symmetrical cell configuration.

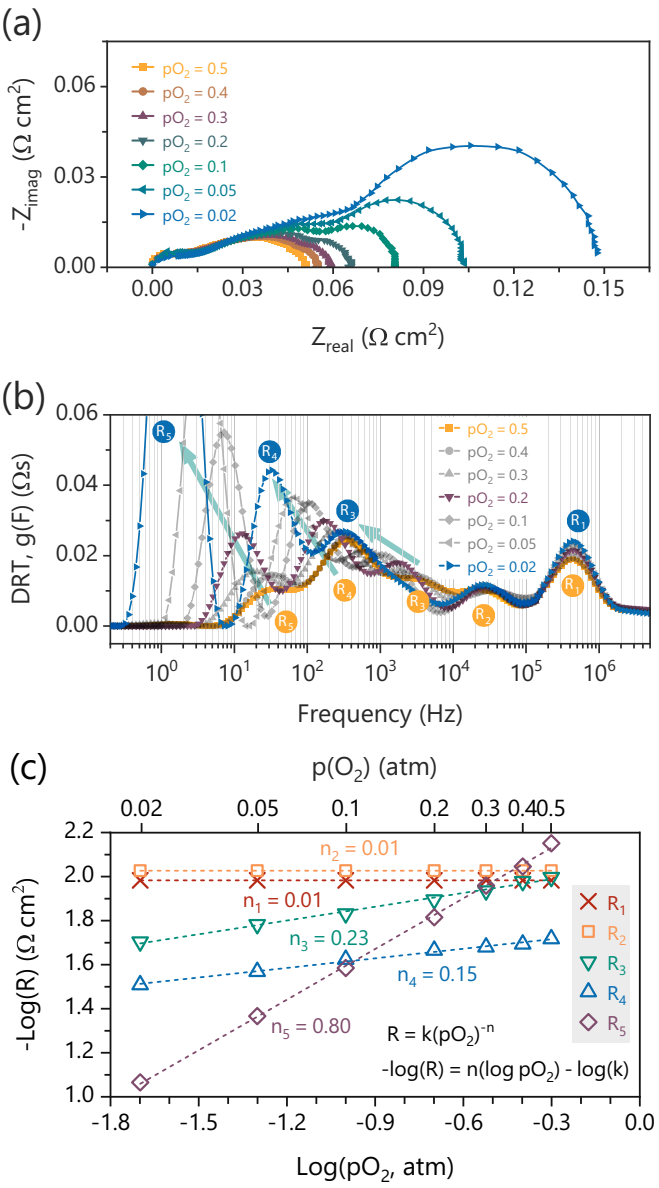

Fig. 7. Oxygen concentration dependency of (a) impedance spectra, (b) corresponding DRTs, and (c) the fitted polarization processes of the LSCF-GDC composite air electrode at 750 °C. Note: the polarization resistance is measured for two electrodes in a symmetrical cell configuration.

constant polarization resistances of 0.010 and 0.009 Ω cm^2, respectively, with a slight standard deviation of 0.0004.

The n-value in the relation $R = k(pO_2)^{-n}$ gives information about the type of species and the underlying electrochemical reaction. The HF processes (R_1Q_1 and R_2Q_2) are almost independent of the oxygen partial pressure. This suggests that R_1Q_1 and R_2Q_2 are not related to an electrochemical reaction. Therefore, the HF peaks with a high activation energy (1.09–1.88 eV) could be interpreted either interfacial oxygen ion transport processes at the GDC/YSZ interface caused by the forming interdiffusion phase during the cell processing [48] or as oxygen ion transfer at the LSCF/GDC interfaces [49]. As the polarization resistance for HF processes remains unchanged when operating the cells with different gas compositions and SO_2 concentrations, it does not affect the current study of poisoning mechanisms in the LSCF-GDC air electrode.

The fitting results at middle frequencies show decreasing resistances with increasing oxygen partial pressure for R_3Q_3 and R_4Q_4. The minimum resistance of $R_3 = 0.010$ Ω cm^2 and $R_4 = 0.019$ Ω cm^2 can be measured for $pO_2 = 0.5$ atm. Based on the concentration dependence for these resistances, reaction orders of $n_3 = 0.23$ and $n_4 = 0.15$ can be determined within the studied oxygen partial pressure range.

There have been various explanations for thermally activated resistances in the middle-frequency range, including dissociative adsorption of oxygen, surface diffusion, and charge transfer on surface reaction sites. The main steps involved in the reaction of oxygen molecules on the LSCF-based electrode surface can be found in the following [12,50]. The adsorption of the oxygen molecules on the electrode surface:

$$O_2\ (gas) \rightarrow O_{2,ads}\ (LSCF) \quad (2)$$

Dissociation of oxygen molecules into oxygen atoms, which are both adsorbed on the surface of the LSCF electrode:

$$O_{2,ads}\ (LSCF) \rightarrow 2O_{ads}\ (LSCF) \quad (3)$$

Dissociation of oxygen molecules into oxygen atoms, which is adsorbed at the electrochemical reaction site on the LSCF* electrode:

$$O_{2,ads}\ (LSCF) \rightarrow 2O_{ads}\ (LSCF^*) \quad (4)$$

Diffusion of adsorbed oxygen atoms (in Eq. 3) to the electrochemical

reaction site (LSCF*):

$$O_{ads}\ (LSCF) \rightarrow O_{ads}\ (LSCF^{*}) \quad (5)$$

The charge transfer reaction on the electrochemical reaction site:

$$O_{ads}\ (LSCF^{*}) + 2e^{'} + V_O^{\bullet\bullet} \rightarrow O_o^{\times}\ (LSCF) \quad (6)$$

After the ORR on the LSCF surface, the incorporated oxygen ions have to be transported through the LSCF bulk and subsequently transferred via the LSCF/GDC interface to a continuous GDC-matrix in the LSCF/GDC-layer and the GDC bulk to the GDC/YSZ interface.

$$O_o^{\times}\ (LSCF) \rightarrow O_o^{\times}\ (LSCF/GDC) \quad (7)$$

$$O_o^{\times}\ (LSCF/GDC) \rightarrow O_o^{\times}\ (GDC/YSZ) \quad (8)$$

Esquirol et al. [51] investigated the concentration dependency of fitted resistances for the $La_{0.6}Sr_{0.4}Co_{0.2}Fe_{0.8}O_3$ electrode while operating at the 500–800 °C temperature range. The study showed that the reaction order varies from 0.13 to 0.23 based on the rate-determining step (r.d.s) in the oxygen reduction reaction. At low temperatures (500–650 °C), the bulk diffusion through the electrode material with $n = 0.13$ is the r.d.s because thermodynamics limits the oxygen vacancy concentration. Meanwhile, the adsorption and surface exchange reactions (it refers to the above equations from 2 to 6) with $n = 0.23$ become the r.d.s at 650 °C, where the kinetics of bulk diffusion through the electrode improves.

Takeda et al. [52] reported a narrow range of reaction order $n = 0.18$–0.26 for the charge transfer to the O_{ads} process by studying the r.d.s for several electrode materials with the perovskite structure. Based on the published values of reaction orders for r.d.s in the literature, it can be concluded that reaction order is highly dependent upon the chemical composition of the electrode material, the morphology and grain size of the catalyst on the electrode surface, and testing temperature [12,38,53,54]. However, it has been established that the charge transfer to O_{ads} is less affected by oxygen partial pressure than the dissociative surface adsorption of oxygen. Accordingly, it appears that the R_3 with a higher dependency on oxygen partial pressure ($n = 0.23$) is most likely associated with the surface dissociation of oxygen molecules into oxygen atoms (Eq. 3 and 4). Meanwhile, the R_4Q_4 with $n = 0.18$ could probably be related to the charge transfer of the O_{ads} on the LSCF surface (Eq. 6).

On the other hand, it is well known from previous studies that the surface reaction on the active material for electrocatalytic reaction (LSCF surface) is strongly correlated with the oxygen ion transport in the bulk of the porose electrode [5]. The simplified serial connection of R_nQ_n elements used for the quantification neglects the coupling of reaction and transport in the porose electrode layer. It should be considered that TLMs like the Gerischer element create a number of subsequent peaks in the DRT, decaying with increasing frequency [55]. Each of these peaks can no longer solely be related to a single reaction or transport process in the electrode, and thus, the general assumption that one peak in the DRT is related to one single surface reaction or transfer process is no longer valid. Accordingly, in another interpretation of impedance spectra, the R_4Q_4 would be dominated by the surface reactions (Eq. 2 to 6), whereas R_3Q_3 is more affected by the oxygen ion diffusion in the LSCF bulk. Due to the coupling of the surface reactions (O_2-adsorption, dissociation, ionization, and transfer to the bulk often summarized in a single oxygen exchange coefficient k) and the oxygen ion diffusion in the electrode bulk, the change of a single parameter will affect size and relaxation frequency of other peaks in the DRT.

Considering the low-frequency process (R_5Q_5), the fit of the spectra reveals a constant, temperature-independent polarization resistance of 0.012 Ω cm^2 in synthetic air over the entire investigated temperature range (Fig. 6c). The concentration dependency of R_5Q_5 at 750 °C shows a significant resistance increase (from 0.007 to 0.086 Ω cm^2) by decreasing pO_2 from 0.5 to 0.002 atm.

The reaction order of $n = 0.80$ reveals the high dependency of the LF process on the oxygen partial pressure. Based on the expected dependence of the gas diffusion resistance on pO_2 [56], the log/log plot should show an even steeper slope of 1.19.

$$R_{D(cathode)} \propto \frac{1}{p_{O_2}} - 1 \quad (9)$$

Despite this minor deviation, it is reasonable to attribute R_5 to gas diffusion through the electrode porosity, the gold mesh, and the rib-flowfield used for contacting the cell. The absolute resistance values are in agreement with previous results obtained in a similar testing setup [57] and have also been observed for impedance spectra of high-performing air electrodes in the intermediate temperature range (650–750 °C) [41].

Fig. 8 shows Nyquist spectra and DRTs, including fits of the serially connected model elements in different gas compositions after operation for 320 h. The same scale of Nyquist plots was used for all the tested cells to demonstrate how SO_2 poisoning affects electrode performance. However, the severe degradation of the LSCF-GDC electrode in 100 ppb SO_2-containing synthetic air with significant polarization resistance would limit a clear illustration of the developing impedance for other measurements. Therefore, the obtained result after 6 h of exposure to SCA-100 with comparable polarization resistance to the aged cell in SA is included. The entire Nyquist plot of the SCA-100 cell after operation for 320 h is available in the supplementary materials (Fig. 1s).

Furthermore, Fig. 8 includes the distribution of relaxation times for aged cells for 320 h and the variation of the DRT during ageing. The initial DRT (0 h) plot of tested LSCF-GDC electrodes in synthetic air is also provided in yellow for each gas composition to compare how the polarization resistance evolves over time. As discussed and shown in Fig. 5, the oxygen reduction reaction for the LSCF-GDC air electrode at 750 °C includes two MF resistances (R_3Q_3 and R_4Q_4).

After operating for 320 h, the SA cell's polarization resistance reaches 0.067 Ω cm^2, and the estimated resistance for R_3Q_3 and R_4Q_4 increases from 0.008 Ω cm^2 to 0.011 Ω cm^2 and from 0.010 Ω cm^2 to 0.021 Ω cm^2, respectively. At the same time, the polarization resistance for the other resistances at HF and LF stays almost at the same level (± 0.001 Ω cm^2). The resistances provided here are for one electrode and must be multiplied by two before being compared with the semi-circle resistances in Fig. 8.

The primary degradation mechanism reported previously for the LSCF electrode in ORR is the Sr enrichment on the LSCF surface, followed by the formation of SrO precipitates [12]. High concentrations of oxygen vacancies and structural defects accelerate the formation of SrO in perovskites [11]. Furthermore, the binding of the cations in the A sites of the perovskite is generally weaker than that of the B sites. As a result, the precipitation of Sr will be more favourable in reducing the excess surface energy created by oxygen vacancy [5]. Consequently, the gradual surface enrichment of SrO with poor electrocatalytic activity and electronic conductivity has a significant detrimental effect on the performance of the LSCF-GDC electrode in long-term operation. The degradation effect is attributed to (i) inhibiting the dissociation of oxygen molecules into oxygen atoms (Eq. 3 and 4), (ii) affecting the surface diffusion of adsorbed oxygen atoms to electrochemical reaction sites (Eq. 5), and (iii) reducing the concentration of electronic species and inhibiting the charge transfer reaction (Eq. 6) [58].

These three detrimental effects are due to SrO precipitates suppressing surface reaction kinetics, known as the surface exchange coefficient (k) in the literature [39]. The degradation of k not only increases the polarization resistance for the electrochemical surface reactions but also its coupling to bulk transport increases the effective resistance for oxide ion transport [59]. Due to a decreased surface exchange rate, the oxygen surface exchange reaction is spread over a more significant part of the electrode volume, which enlarges the penetration depth or average diffusion length.

The results in synthetic air show that the primary increasing resistance is R_4Q_4 (Fig. 8a), while a slight increase in R_3Q_3 can also be

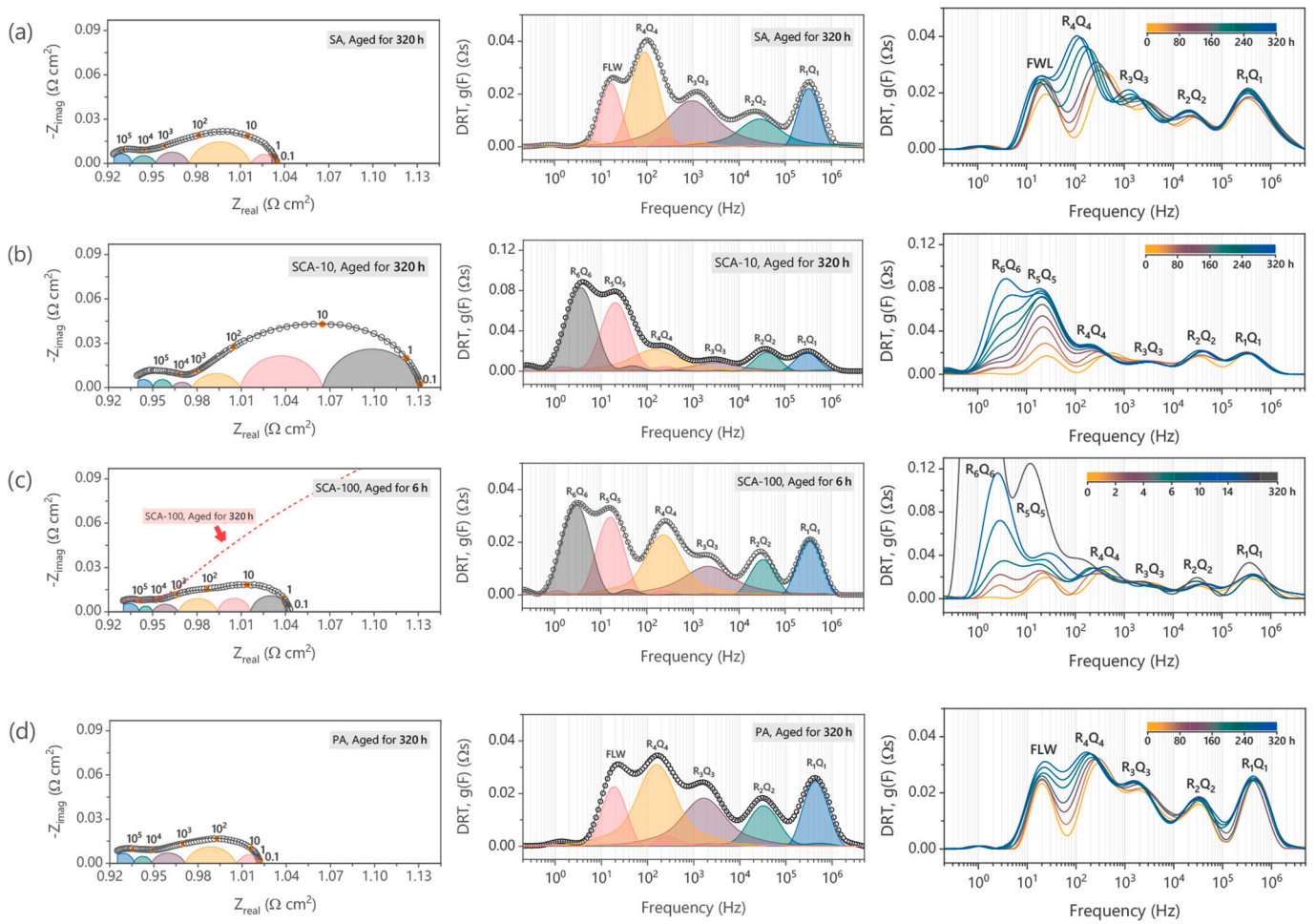

Fig. 8. Impedance spectra and DRT of the LSCF-GDC air electrode at 750 °C for investigated cells in (a) synthetic air (SA), (b) 10 ppb SO_2-containing air (SCA-10), (c) 100 ppb SO_2-containing air (SCA-100), and (d) purified 100 ppb SO_2-containing air (PA). Note: the polarization resistance is measured for two LSCF-GDC electrodes in a symmetrical cell configuration.

observed. Both MF peaks shift toward lower frequencies as resistance increases. This is a typical electrochemical reaction degradation behaviour with an approximately constant capacitive contribution. The capacitive contribution in R_3Q_3 is related to the chemical capacity of the LSCF bulk, which is assumed to undergo only minor changes during 320 h. Considering that R_4Q_4 is related to degrading reactions at the LSCF surface, whereas the capacitive contribution Q_4 is related to the chemical capacitance of LSCF and is thus unaffected.

In the case of R_3Q_3, two different interpretations are feasible. If R_3Q_3 is assumed to be a subsequent reaction step on the LSCF surface, a qualitatively similar behaviour as observed for R_4Q_4 is to be expected. Considering a Gerischer-type behaviour, R_3Q_3 represents the second peak of the Gerischer element in the DRT, resulting from the coupling of surface reaction and bulk transport. Even if the bulk transport, i.e., the oxygen ion diffusion coefficient in the LSCF, is not affected, the observed change of the two peaks in the DRT appears because the overall resistance R_{chem} and the time constant t_{chem} of the Gerischer element are both affected by reciprocal surface exchange coefficient (k^{δ}) [39].

Similarly, the electrochemical performance of the LSCF-GDC electrode is investigated for synthetic air containing 10 and 100 ppb SO_2, i.e., SCA-10 and SCA-100. The impedance spectra indicate a significant degradation of the polarization resistance caused by trace amounts of SO_2 in synthetic air (Fig. 8b and c). Accordingly, the R_p increases from about 0.03 Ω cm^2 to 0.123 Ω cm^2 and 0.257 Ω cm^2 after testing for 320 h in SCA-10 and SCA-100, respectively.

The SCA-10 and SCA-100 results reveal that the electrode performance is primarily limited by an initially strongly growing peak at 20 Hz (R_5Q_5 previously related to the gas diffusion (FLW)) and later on an additional process (R_6Q_6) at lower frequencies with a relaxation frequency of about 3 Hz (Fig. 8b). Considering that the gas diffusion inside contact mesh, flow field, and electrode porosity does not change due to SO_2 during the 320 h of testing (Fig. 3a to 3c), such severe increase in gas diffusion polarization can be excluded. This represents an interfering relaxation frequency at low frequencies for the resistances involved in the oxygen reduction reaction. To provide a reasonable interpretation of the impedance results for the cells tested in SO_2-containing air, the FLW element was replaced with an RQ element. However, gas diffusion resistance still percolates in polarization resistance, but it is difficult to distinguish it from other low-frequency resistances.

The DRT plots show a high contribution of R_6Q_6 to the polarization resistance for both gas compositions. As a result, increasing the SO_2 concentration to 100 ppb coincides with a severe degradation rate in the LSCF-GDC electrode. Accordingly, 6 h of operation in SCA-100 causes an increase in polarization resistance to similar values as those obtained for the SA cell after 320 h (Fig. 8c). For better illustrating the evolution rate of low-frequency resistance (R_6Q_6), the variation of DRT curves is zoomed to the early stages of the degradation study for the SCA-100 cell, and the corresponding DRT plot after 320 h has been plotted on top. The resistance of R_6Q_6 after 6 h of operation reaches 0.027 Ω cm^2 and becomes the rate-determining reaction in the electrochemical performance of LSCF-GDC electrodes in the SCA atmosphere, covering 76% of total polarization resistance after 320 h.

According to previous studies, the degradation of electrocatalytic reaction on the electrode surface is caused by the trace amount of air impurities dominating the electrochemical performance at intermediate operation temperatures (650–750 °C) [10,60]. The degradation mechanism at low concentrations of SO_2 (in the range of 1–10 ppb) is predominantly due to the deactivation of electrochemically active sites by the occupation of SO_2 in the oxide ion vacancies and subsequent formation of SO_3^{2-} on the LSCF surface [61,62]. At the same time, no changes have been observed in the chemical composition and microstructure of electrode material, with no evidence forming the $SrSO_4$ phase [14], primarily when operating at open circuit voltage [63,64]. The adsorbed SO_2 molecules on the LSCF grain surface will inhibit the O_2 adsorption (Eq. 2) or hinder the surface diffusion for adsorbed oxygen atoms (Eq. 5) to reach electrochemical reaction sites [10].

In other words, the R_6Q_6 at low frequency, as the rate-determining step in the SCA atmosphere, is most likely related to the adsorption of the oxygen molecules on the LSCF surface. Meanwhile, the R_5Q_5 process could be related to the surface diffusion of O_{ads} to pass over passivated regions caused by forming SrO, SO_3^{2-}, and $SrSO_4$ phases [58]. The diffusion of O_{ads} can occur through the passive layer after ionization. However, to the authors' knowledge, no evidence is reported in the literature for this type of transport.

On the other hand, overlapping the gas diffusion (FLW) and the O_{ads} surface diffusion processes with close relaxation frequency limits their distinguishment for the SCA cell. As the gas diffusion process is rather small and no changes are expected, only one R_5Q_5 element is considered and attributed to the surface diffusion processes in the SCA-10 and SCA-100 cells.

With respect to a Gerischer-based modeling approach, it has to be considered that the severe impact of sulfur on the surface exchange will increase the penetration depth, and a value exceeding the thickness of the electrode can be achieved. Under these conditions (very low surface exchange rate at still high oxygen ion diffusion coefficient), the oxygen ion diffusion resistance in the LSCF and GDC bulk becomes negligible, and processes at the LSCF surface dominate the impedance.

The DRT plot in Fig. 8c shows a higher degradation rate for the SCA-100 compared to the SCA-10. Increasing SO_2 concentration in SCA-100 can cause microstructural changes and accelerate the formation of sulfur species on the electrode surface. However, the amount of reaction product in sulfur poisoning of the experimental results is lower than predicted by thermodynamic calculation, which can be attributed to kinetic effects according to Eq. 10.

$$\mathrm{SrO\ (in\ the\ LSCF\ electrode)} + \mathrm{SO_2\ (g)} + 0.5\mathrm{O_2\ (g)} = \mathrm{SrSO_4} \quad (10)$$

The $SrSO_4$ formation highly depends on the concentration of gaseous reactants and the activity of SrO as the plausible reaction sites [65]. Besides, increasing the flow rate for the SO_2/air mixture can accelerate the reaction kinetics [58].

As shown in the postmortem FIB/SEM analysis (Fig. 2), a high concentration of $SrSO_4$ forms at the outer region of the LSCF-GDC electrode (marked with (α)) after operating in the SCA-100 for 320 h, which was not the case for the SCA-10. The corresponding SEM and EDS images for the SCA-10 are provided in the supplementary material (Fig. 2s). High contamination of perovskite with SO_2 impurities can further suppress the electrocatalytic reaction and increase the adsorption resistance of the oxygen molecules and diffusion path through/over passive layer due to the formation of extended $SrSO_4$ layer [32]. Consequently, the polarization resistance of corresponding reactions, R_5Q_5 and R_6Q_6, significantly increases under 100 ppb SO_2-containing synthetic air.

As a final step in studying the degradation mechanisms of the electrochemical performance of the LSCF-GDC electrode in different air compositions, the developed filter material has been installed in the inlet gas channel to purify the SCA-100. Fig. 8d shows the impedance spectrum and DRT plot for the purified SCA-100 (PA). The obtained results show that the electrode performance primarily degrades due to increasing polarization resistance for the R_4Q_4 process, besides slightly increasing the resistance for the R_3Q_3, which is similar to degradation mechanisms observed for the SA cell. The comparable polarization resistance observed in PA and SA cells with similar degradation mechanisms highlights the practical application of the developed filter in mitigating surface deactivation caused by SO_2 poisoning. Consequently, employing the current filter to absorb ambient air impurities can prolong the electrochemical performance lifespan of the LSCF-GDC air electrode in commercial stacks.

4. Conclusion

This work covers the electrochemical performance of the LSCF-GDC composite air electrode under synthetic air containing different amounts of SO_2, followed by examining the effectiveness of the developed filter material in adsorbing this air impurity while measuring impedance spectra at 750 °C for 320 h. Accordingly, the degradation of LSCF-GDC electrodes in synthetic air was compared to ones containing 10 and 100 ppb SO_2, and the degradation mechanism under filtered air with 100 ppb SO_2 was investigated.

The impedance spectra showed a low intrinsic initial degradation rate of 0.05 mΩ cm^2 h^{-1} for the tested cell in synthetic air while exposing the LSCF-GDC electrode to the 10 and 100 ppb SO_2-containing air, causing a severe increase of degradation rate to 0.17 and 0.30 mΩ cm^2 h^{-1}, respectively. Nevertheless, the calculated degradation rate for the tested cell in the purified air was similar to the intrinsic degradation rate of the LSCF-GDC electrode, showing the high efficiency of the filter material in adsorbing SO_2.

The deconvoluted processes using the distribution of relaxation times (DRT) method showed that the oxygen reduction reaction for the LSCF-GDC electrode consists of two thermally activated processes at middle frequencies and one strongly oxygen concentration-dependent reaction at low frequencies. Based on the fitting results, the main degradation mechanisms in synthetic air were the limitation of surface reactions, including the dissociative surface adsorption of oxygen, surface diffusion of adsorbed oxygen, and interfacial charge transfer due to the formation of the insulator SrO phase.

The DRT analysis of the tested cell under SO_2-containing air revealed another resistance at lower frequencies with a high degradation rate. The corresponding resistance was estimated at 0.195 Ω cm^2 after operation for 320 h, covering 76% of the total polarization resistance for the LSCF-GDC electrode. This degradation mechanism is most likely due to the formation of SrO, SO_3^{2-}, and $SrSO_4$ phases, which significantly inhibit O_2 adsorption on the LSCF surface. Further, the presence of a passive layer might require the O_{ads} to pass over the deactivated region after ionization. Consequently, the diffusion path could be through the formed phases or along with the passive layer to electrochemically active sites on the LSCF surface.

The application of the filter material (MANN+HUMMEL Innenraumfilter GmbH & Co. KG) proved its suitability in SO_2 removal. A degradation rate for the tested cell in the purified air previously containing 100 ppb SO_2 was similar to the intrinsic degradation rate of the LSCF-GDC electrode, highlighting the impressive ability of the filter material to capture air contaminants and prolong the lifespan of SOCs.

Author contributions (according to CRediT author statement)

Yousef Alizad Farzin: Writing - Original Draft, Conceptualization, Visualization, Methodology, Formal Analysis, Validation, Investigation.

Michael Harenbrock: Writing - Review & Editing, Resources.

David Nardini: Writing - Review & Editing, Resources.

André Weber: Writing - Review & Editing, Validation, Supervision, Project administration, Funding acquisition, Resources.

CRediT authorship contribution statement

Yousef Alizad Farzin: Writing – original draft, Validation,

Investigation, Formal analysis. **Michael Harenbrock:** Writing – review & editing, Resources. **David Nardini:** Writing – review & editing, Resources. **André Weber:** Writing – review & editing, Supervision, Resources, Project administration, Conceptualization.

Declaration of competing interest

The authors declare the following financial interests/personal relationships which may be considered as potential competing interests:

Yousef Alizad Farzin reports financial support was provided by The Federal Ministry of Education and Research (BMBF). Yousef Alizad Farzin reports equipment, drugs, or supplies was provided by Sunfire GmbH. If there are other authors, they declare that they have no known competing financial interests or personal relationships that could have appeared to influence the work reported in this paper.

Data availability

Data will be made available on request.

Acknowledgements

The authors gratefully acknowledge funding from the Federal Ministry of Education and Research (BMBF 03SF0621G). We would like to thank Sunfire GmbH for providing the LSCF-GDC air electrode. In addition, the authors would like to express their appreciation to Annette Schucker for her technical assistance with FIB-SEM microscopy at KIT (IAM-ET).

Appendix A. Supplementary data

Supplementary data to this article can be found online at https://doi.org/10.1016/j.ssi.2024.116569.

References

[1] S. Biswas, G. Kaur, G. Paul, S. Giddey, A critical review on cathode materials for steam electrolysis in solid oxide electrolysis, Int. J. Hydrog. Energy (2023), https://doi.org/10.1016/J.IJHYDENE.2022.11.307.

[2] Y. Alizad Farzin, M. Bjerg Mogensen, S. Pirou, H. Lund Frandsen, Perovskite/Ruddlesden-popper composite fuel electrode of strontium-praseodymium-manganese oxide for solid oxide cells: an alternative candidate, J. Power Sources 580 (2023) 233450, https://doi.org/10.1016/j.jpowsour.2023.233450.

[3] Y. Alizad Farzin, A. Babaei, T. Løye Skafte, E. Stamate, A. Ataie, S.H. Jensen, Development of an SFMM/CGO composite electrode with stable electrochemical performance at different oxygen partial pressures, Int. J. Hydrog. Energy 47 (2022) 7915–7931, https://doi.org/10.1016/J.IJHYDENE.2021.12.104.

[4] Y.A. Farzin, A. Babaei, T.L. Skafte, E. Stamate, A. Ataie, S.H. Jensen, Low-temperature preparation and investigation of electrochemical properties of SFM/CGO composite electrode, Solid State Ionics 356 (2020) 115435, https://doi.org/10.1016/j.ssi.2020.115435.

[5] S.P. Jiang, Development of lanthanum strontium cobalt ferrite perovskite electrodes of solid oxide fuel cells – a review, Int. J. Hydrog. Energy 44 (2019) 7448–7493, https://doi.org/10.1016/j.ijhydene.2019.01.212.

[6] S.D. Safian, N.I. Abd Malek, Z. Jamil, S.W. Lee, C.J. Tseng, N. Osman, Study on the surface segregation of mixed ionic-electronic conductor lanthanum-based perovskite oxide La1−xSrxCo1−yFeyO3−δ materials, Int. J. Energy Res. 46 (2022) 7101–7117, https://doi.org/10.1002/ER.7733.

[7] A. Mai, V.A.C. Haanappel, F. Tietz, D. Stöver, Ferrite-based perovskites as cathode materials for anode-supported solid oxide fuel cells: part II. Influence of the CGO interlayer, Solid State Ionics 177 (2006) 2103–2107, https://doi.org/10.1016/J.SSI.2005.12.010.

[8] F.E. Winterhalder, Y. Alizad Farzin, O. Guillon, A. Weber, N.H. Menzler, Perovskite-based materials as alternative fuel electrodes for solid oxide electrolysis cells (SOECs), ECS Trans. 111 (2023) 1115–1123, https://doi.org/10.1149/11106.1115ecst.

[9] Y.A. Farzin, A. Weber, M. Harenbrock, D. Nardini, Effective suppression of LSCF air electrode degradation by air cleaning, ECS Trans. 111 (2023) 1987, https://doi.org/10.1149/11106.1987ECST.

[10] F. Wang, H. Kishimoto, T. Ishiyama, K. Develos-Bagarinao, K. Yamaji, T. Horita, H. Yokokawa, A review of sulfur poisoning of solid oxide fuel cell cathode materials for solid oxide fuel cells, J. Power Sources 478 (2020) 228763, https://doi.org/10.1016/j.jpowsour.2020.228763.

[11] M. Anwar, M.A. Shaikh Abdul, U.M. Khan, M. Hassan, A.H. Khoja, A. Muchtar, A review of X-ray photoelectron spectroscopy technique to analyze the stability and degradation mechanism of solid oxide fuel cell cathode materials, Materials (Basel). 15 (2022) 2540, https://doi.org/10.3390/ma15072540.

[12] D. Oh, D. Gostovic, E.D. Wachsman, Mechanism of La0.6Sr0.4Co0.2Fe0.8O3 cathode degradation, J. Mater. Res. 27 (2012) 1992–1999, https://doi.org/10.1557/JMR.2012.222.

[13] C. Endler-Schuck, A. Leonide, A. Weber, S. Uhlenbruck, F. Tietz, E. Ivers-Tiffée, Performance analysis of mixed ionic–electronic conducting cathodes in anode supported cells, J. Power Sources 196 (2011) 7257–7262, https://doi.org/10.1016/J.JPOWSOUR.2010.11.079.

[14] S.S. Liu, K. Develos-Bagarinao, R.A. Budiman, T. Ishiyama, H. Kishimoto, K. Yamaji, Towards an atomic scale understanding of the early-stage deterioration mechanism of LSCF, J. Mater. Chem. A 11 (2023) 21983–22000, https://doi.org/10.1039/D3TA04585D.

[15] C.C. Wang, K. Chen, S.P. Jiang, Sulfur deposition and poisoning of La 0.6 Sr 0.4 co 0.2 Fe 0.8 O 3-δ cathode materials of solid oxide fuel cells, J. Electrochem. Soc. 161 (2014) F1133–F1139, https://doi.org/10.1149/2.0041412JES/XML.

[16] H. Yokokawa, Y. Hori, T. Shigehisa, M. Suzuki, S. Inoue, T. Suto, K. Tomida, M. Shimazu, A. Kawakami, H. Sumi, M. Ohmori, N. Mori, T. Iha, K. Yamaji, H. Kishimoto, K. Develos-Bagarinao, K. Sasaki, S. Taniguchi, T. Kawada, M. Muramatsu, K. Terada, K. Eguchi, T. Matsui, H. Iwai, M. Kishimoto, N. Shikazono, Y. Mugikura, T. Yamamoto, M. Yoshikawa, K. Yasumoto, K. Asano, Y. Matsuzaki, S. Amaha, T. Somekawa, Recent achievements of NEDO durability project with an emphasis on correlation between cathode Overpotential and Ohmic loss, Fuel Cells 17 (2017) 473–497, https://doi.org/10.1002/FUCE.201600186.

[17] H. Yokokawa, M. Suzuki, M. Yoda, T. Suto, K. Tomida, K. Hiwatashi, M. Shimazu, A. Kawakami, H. Sumi, M. Ohmori, T. Ryu, N. Mori, M. Iha, S. Yatsuzuka, K. Yamaji, H. Kishimoto, K. Develos-Bagarinao, T. Shimonosono, K. Sasaki, S. Taniguchi, T. Kawada, M. Muramatsu, K. Terada, K. Eguchi, T. Matsui, H. Iwai, M. Kishimoto, N. Shikazono, Y. Mugikura, T. Yamamoto, M. Yoshikawa, K. Yasumoto, K. Asano, Y. Matsuzaki, K. Sato, T. Somekawa, Achievements of NEDO durability projects on SOFC stacks in the light of physicochemical mechanisms, Fuel Cells 19 (2019) 311–339, https://doi.org/10.1002/FUCE.201800187.

[18] S.D. Safian, N.I. Abd Malek, Z. Jamil, S. Lee, C. Tseng, N. Osman, Study on the surface segregation of mixed ionic-electronic conductor lanthanum-based perovskite oxide <scp> La 1−x Sr x Co 1−y Fe y O 3− </scp> δ materials, Int. J. Energy Res. 46 (2022) 7101–7117, https://doi.org/10.1002/er.7733.

[19] R.A. Budiman, S.S. Liu, K.D. Bagarinao, T. Ishiyama, H. Kishimoto, K. Yamaji, T. Horita, H. Yokokawa, Determination of factors governing surface composition and degradation of La 0.6 Sr 0.4 Co 0.2 Fe 0.8 O 3- δ electrode under sulfur-contained air, J. Electrochem. Soc. 166 (2019) F414–F422, https://doi.org/10.1149/2.0091906JES/XML.

[20] F. Wang, K. Yamaji, D.-H. Cho, T. Shimonosono, H. Kishimoto, M.E. Brito, T. Horita, H. Yokokawa, Sulfur poisoning on La0.6Sr0.4Co0.2Fe0.8O3 cathode for SOFCs, J. Electrochem. Soc. 158 (2011) B1391, https://doi.org/10.1149/2.059111JES/XML.

[21] K. Gao, X. Liu, Z. Wang, C. Liang, Y. Xiong, An effective approach to protect the Sm 0.5 Sr 0.5 Co 3−δ (SSC) cathode from SO 2 in SOFCs, RSC Adv 6 (2016) 42447–42451, https://doi.org/10.1039/C6RA05309B.

[22] C.C. Wang, D. Luo, B. Hou, S.P. Jiang, Effect of BaO impregnation on sulfur tolerance of La 0.6 Sr 0.4 co 0.2 Fe 0.8 O 3− δ cathodes of solid oxide fuel cells, Mater. Res. Express. 6 (2019) 075504, https://doi.org/10.1088/2053-1591/ab1122.

[23] C.C. Wang, D. Luo, S.P. Jiang, B. Lin, Highly sulfur poisoning-tolerant BaCeO 3 -impregnated La 0.6 Sr 0.4 Co 0.2 Fe 0.8 O 3− δ cathodes for solid oxide fuel cells, J. Phys. D, Appl. Phys. 51 (2018) 435502, https://doi.org/10.1088/1361-6463/aadf4c.

[24] C. Berger, E. Bucher, C. Gspan, A. Menzel, W. Sitte, Impact of SO 2 on the oxygen exchange kinetics of the promising SOFC/SOEC air electrode material La 0.8 Ca 0.2 FeO 3-δ, J. Electrochem. Soc. 164 (2017) F3008–F3018, https://doi.org/10.1149/2.0041710JES/XML.

[25] C. Berger, E. Bucher, C. Gspan, A. Menzel, W. Sitte, Long-term stability of oxygen surface exchange kinetics of Pr0.8Ca0.2FeO3-δ against SO2-poisoning, Solid State Ionics 326 (2018) 82–89, https://doi.org/10.1016/J.SSI.2018.09.017.

[26] M. Harenbrock, A. Korn, A. Weber, E. Hallbauer, Cost-Efficient Cathode Air Path for PEM Fuel Cell Systems, SAE Tech. Pap. 2020-April, 2020, https://doi.org/10.4271/2020-01-1176.

[27] D. Klotz, A. Weber, E. Ivers-Tiffée, Practical guidelines for reliable electrochemical characterization of solid oxide fuel cells, Electrochim. Acta 227 (2017) 110–126, https://doi.org/10.1016/J.ELECTACTA.2016.12.148.

[28] S. Dierickx, A. Weber, E. Ivers-Tiffée, How the distribution of relaxation times enhances complex equivalent circuit models for fuel cells, Electrochim. Acta 355 (2020) 136764, https://doi.org/10.1016/J.ELECTACTA.2020.136764.

[29] C.C. Wang, S. He, K. Chen, M.R. Rowles, S. Darvish, Y. Zhong, S.P. Jiang, Effect of SO 2 poisoning on the electrochemical activity of La 0.6 Sr 0.4 co 0.2 Fe 0.8 O 3-δ cathodes of solid oxide fuel cells, J. Electrochem. Soc. 164 (2017) F514–F524, https://doi.org/10.1149/2.0421706JES/XML.

[30] Y.A. Farzin, I. Ritucci, B. Talic, R. Kiebach, H.L. Frandsen, Fracture toughness of reactive bonded co–Mn and cu–Mn contact layers after long-term aging, Ceram. Int. 48 (2022) 20699–20711, https://doi.org/10.1016/J.CERAMINT.2022.04.050.

[31] A. Girard, M. Stekiel, D. Spahr, W. Morgenroth, B. Wehniger, V. Milman, A. Tra Nguyen-Thanh, A. Mirone, L. Minelli, A. Paolasini, W. Bjoern Bosak, Structural, elastic and vibrational properties of celestite, SrSO4, from synchrotron x-ray diffraction, thermal diffuse scattering and Raman scattering, J. Phys. Condens. Matter 31 (2018) 055703, https://doi.org/10.1088/1361-648X/AAF0EF.

[32] M. Krammer, A. Schmid, A. Nenning, A.E. Bumberger, M. Siebenhofer, C. Herzig, A. Limbeck, C. Rameshan, M. Kubicek, J. Fleig, Closed-pore formation in oxygen electrodes for solid oxide electrolysis cells investigated by impedance spectroscopy, ACS Appl. Mater. Interfaces 15 (2023) 8076–8092, https://doi.org/10.1021/ACSAMI.2C20731/ASSET/IMAGES/LARGE/AM2C20731_0017.JPEG.
[33] J. Laurencin, M. Hubert, D.F. Sanchez, S. Pylypko, M. Morales, A. Morata, B. Morel, D. Montinaro, F. Lefebvre-Joud, E. Siebert, Degradation mechanism of La0.6Sr0.4Co0.2Fe0.8O3-δ/Gd0.1Ce0.9O2-δ composite electrode operated under solid oxide electrolysis and fuel cell conditions, Electrochim. Acta 241 (2017) 459–476, https://doi.org/10.1016/J.ELECTACTA.2017.05.011.
[34] A. Tsoga, A. Naoumidis, D. Stöver, Total electrical conductivity and defect structure of ZrO2–CeO2–Y2O3–Gd2O3 solid solutions, Solid State Ionics 135 (2000) 403–409, https://doi.org/10.1016/S0167-2738(00)00477-X.
[35] F. Wankmüller, J. Szász, J. Joos, V. Wilde, H. Störmer, D. Gerthsen, E. Ivers-Tiffée, Correlative tomography at the cathode/electrolyte interfaces of solid oxide fuel cells, J. Power Sources 360 (2017) 399–408, https://doi.org/10.1016/J.JPOWSOUR.2017.06.008.
[36] J. Szász, F. Wankmüller, V. Wilde, H. Störmer, D. Gerthsen, N.H. Menzler, E. Ivers-Tiffée, Nature and functionality of La0.58Sr0.4Co0.2Fe0.8O3-δ / Gd0.2Ce0.8O2-δ / Y0.16Zr0.84O2-δ interfaces in SOFCs, J. Electrochem. Soc. 165 (2018) F898, https://doi.org/10.1149/2.0031811JES.
[37] K. Chen, S.P. Jiang, Surface Segregation in Solid Oxide Cell Oxygen Electrodes: Phenomena, Mitigation Strategies and Electrochemical Properties, Electrochem. Energy Rev. 2020 34. 3 (2020) 730–765. doi:https://doi.org/10.1007/S41918-020-00078-Z.
[38] P. Costamagna, E.M. Sala, W. Zhang, M. Lund Traulsen, P., Holtappels, electrochemical impedance spectroscopy of La0.6Sr0.4Co0.2Fe0.8O3-δ nanofiber cathodes for intermediate temperature-solid oxide fuel cell applications: a case study for the 'depressed' or 'fractal' Gerischer element, Electrochim. Acta 319 (2019) 657–671, https://doi.org/10.1016/J.ELECTACTA.2019.06.068.
[39] C. Endler-Schuck, J. Joos, C. Niedrig, A. Weber, E. Ivers-Tiffée, The chemical oxygen surface exchange and bulk diffusion coefficient determined by impedance spectroscopy of porous La0.58Sr0.4Co0.2Fe0.8O3−δ (LSCF) cathodes, Solid State Ionics 269 (2015) 67–79, https://doi.org/10.1016/j.ssi.2014.11.018.
[40] F. Monaco, D. Ferreira-Sanchez, M. Hubert, B. Morel, D. Montinaro, D. Grolimund, J. Laurencin, Oxygen electrode degradation in solid oxide cells operating in electrolysis and fuel cell modes: LSCF destabilization and interdiffusion at the electrode/electrolyte interface, Int. J. Hydrog. Energy 46 (2021) 31533–31549, https://doi.org/10.1016/j.ijhydene.2021.07.054.
[41] J. Nielsen, T. Jacobsen, M. Wandel, Impedance of porous IT-SOFC LSCF:CGO composite cathodes, Electrochim. Acta 56 (2011) 7963–7974, https://doi.org/10.1016/J.ELECTACTA.2011.05.042.
[42] S.B. Adler, J.A. Lane, B.C.H. Steele, Electrode kinetics of porous mixed-conducting oxygen electrodes, J. Electrochem. Soc. 143 (1996) 3554–3564, https://doi.org/10.1149/1.1837252.
[43] J. Nielsen, P. Hjalmarsson, M.H. Hansen, P. Blennow, Effect of low temperature in-situ sintering on the impedance and the performance of intermediate temperature solid oxide fuel cell cathodes, J. Power Sources 245 (2014) 418–428, https://doi.org/10.1016/J.JPOWSOUR.2013.06.067.
[44] P. Hjalmarsson, M. Søgaard, M. Mogensen, Oxygen transport properties of dense and porous (La0.8Sr0.2)0.99Co0.8Ni0.2O3-δ, Solid State Ionics 180 (2009) 1290–1297, https://doi.org/10.1016/J.SSI.2009.07.012.
[45] B.A. Boukamp, M. Verbraeken, D.H.A. Blank, P. Holtappels, SOFC-anodes, proof for a finite-length type Gerischer impedance? Solid State Ionics 177 (2006) 2539–2541, https://doi.org/10.1016/J.SSI.2006.03.002.
[46] S. Dierickx, J. Joos, A. Weber, E. Ivers-Tiffée, Advanced impedance modelling of Ni/8YSZ cermet anodes, Electrochim. Acta 265 (2018) 736–750, https://doi.org/10.1016/J.ELECTACTA.2017.12.029.
[47] S. Dierickx, A. Weber, E. Ivers-Tiffée, How the distribution of relaxation times enhances complex equivalent circuit models for fuel cells, Electrochim. Acta 355 (2020) 136764, https://doi.org/10.1016/J.ELECTACTA.2020.136764.
[48] F. Kullmann, C. Grosselindemann, L. Salamon, F.M. Fuchs, A. Weber, Impedance analysis of electrolyte processes in a solid oxide cell, Fuel Cells 23 (2023) 420–429, https://doi.org/10.1002/FUCE.202300035.
[49] F. Qiang, K.N. Sun, N.Q. Zhang, X.D. Zhu, S.R. Le, D.R. Zhou, Characterization of electrical properties of GDC doped A-site deficient LSCF based composite cathode using impedance spectroscopy, J. Power Sources 168 (2007) 338–345, https://doi.org/10.1016/J.JPOWSOUR.2007.03.040.
[50] S.B. Adler, Mechanism and kinetics of oxygen reduction on porous La1-xSrxCoO3-δ electrodes, Solid State Ionics 111 (1998) 125–134, https://doi.org/10.1016/s0167-2738(98)00179-9.
[51] A. Esquirol, N.P. Brandon, J.A. Kilner, M. Mogensen, Electrochemical characterization of La0.6Sr0.4Co0.2Fe0.8 O 3 cathodes for intermediate-temperature SOFCs, J. Electrochem. Soc. 151 (2004) A1847, https://doi.org/10.1149/1.1799391.
[52] Y. Takeda, R. Kanno, M. Noda, Y. Tomida, O. Yamamoto, Cathodic polarization phenomena of perovskite oxide electrodes with stabilized zirconia, J. Electrochem. Soc. 134 (1987) 2656–2661, https://doi.org/10.1149/1.2100267.
[53] C. Xiong, J.A. Taillon, C. Pellegrinelli, Y.-L. Huang, L.G. Salamanca-Riba, B. Chi, L. Jian, J. Pu, E.D. Wachsman, Long-term Cr poisoning effect on LSCF-GDC composite cathodes sintered at different temperatures, J. Electrochem. Soc. 163 (2016) F1091–F1099, https://doi.org/10.1149/2.0841609JES/XML.
[54] J.D. Kim, G.D. Kim, J.W. Moon, Y. Il Park, W.H. Lee, K. Kobayashi, M. Nagai, C. E. Kim, Characterization of LSM–YSZ composite electrode by ac impedance spectroscopy, Solid State Ionics 143 (2001) 379–389, https://doi.org/10.1016/S0167-2738(01)00877-3.
[55] A. Weber, Impedance analysis of porous electrode structures in batteries and fuel cells Impedanzanalyse poröser Elektrodenstrukturen in Batterien und Brennstoffzellen, Tech. Mess. 88 (2021) 1–16, https://doi.org/10.1515/TEME-2020-0084/ASSET/GRAPHIC/J_TEME-2020-0084_FIG_001.JPG.
[56] J. Kim, A.V. Virkar, K. Fung, K. Mehta, S.C. Singhal, Polarization effects in intermediate temperature, anode-supported solid oxide fuel cells, J. Electrochem. Soc. 146 (1999) 69–78, https://doi.org/10.1149/1.1391566/XML.
[57] A. Leonide, V. Sonn, A. Weber, E. Ivers-Tiffée, Evaluation and modeling of the cell resistance in anode-supported solid oxide fuel cells, J. Electrochem. Soc. 155 (2008) B36, https://doi.org/10.1149/1.2801372.
[58] F. Wang, K. Yamaji, D.-H. Cho, T. Shimonosono, H. Kishimoto, M.E. Brito, T. Horita, H. Yokokawa, Sulfur poisoning on La0.6Sr0.4Co0.2Fe0.8O3 cathode for SOFCs, J. Electrochem. Soc. 158 (2011) B1391, https://doi.org/10.1149/2.059111JES/XML.
[59] De R. Souza, J. Kilner, Oxygen transport in La1−xSrxMn1−yCoyO3±δ perovskites, Solid State Ionics 126 (1999) 153–161, https://doi.org/10.1016/S0167-2738(99)00228-3.
[60] F. Wang, H. Kishimoto, K. Develos-Bagarinao, K. Yamaji, T. Horita, H. Yokokawa, Interrelation between sulfur poisoning and performance degradation of LSCF cathode for SOFCs, J. Electrochem. Soc. 163 (2016) F899–F904, https://doi.org/10.1149/2.1151608JES/XML.
[61] R. Wang, L.R. Parent, S. Gopalan, Y. Zhong, Experimental and computational investigations on the SO2 poisoning of (La0.8Sr0.2)0.95MnO3 cathode materials, Adv. Powder Mater. 2 (2023) 100062, https://doi.org/10.1016/J.APMATE.2022.100062.
[62] F. Wang, K. Yan, R.A. Budiman, H. Kishimoto, T. Ishiyama, K.D. Bagarinao, K. Yamaji, T. Horita, H. Yokokawa, Effect of operating temperature on sulfur distribution and performance degradation of porous La0.6Sr0.4Co0.2Fe0.8O3−δ electrode, J. Electrochem. Soc. 167 (2020) 114507, https://doi.org/10.1149/1945-7111/ABA4E9.
[63] J. Xie, Y.W. Ju, T. Ishihara, Influence of sulfur impurities on the stability of La0.6Sr0.4Co0.2Fe0.8O3 cathode for solid oxide fuel cells, Solid State Ionics 249–250 (2013) 177–183, https://doi.org/10.1016/J.SSI.2013.08.005.
[64] F. Wang, K. Yamaji, D.-H. Cho, T. Shimonosono, M. Nishi, H. Kishimoto, M.E. Brito, T. Horita, H. Yokokawa, Evaluation of sulfur dioxide poisoning for LSCF cathodes, Fuel Cells 13 (2013) 520–525, https://doi.org/10.1002/fuce.201200172.
[65] F. Wang, K. Yamaji, D.H. Cho, T. Shimonosono, M. Nishi, H. Kishimoto, M.E. Brito, T. Horita, H. Yokokawa, Evaluation of sulfur dioxide poisoning for LSCF cathodes, Fuel Cells 13 (2013) 520–525, https://doi.org/10.1002/FUCE.201200172.